

# Manifold Learning in MR Spectroscopy Using Nonlinear Dimensionality Reduction and Unsupervised Clustering

Guang Yang,\* Felix Raschke, Thomas R. Barrick, and Franklyn A. Howe

**Purpose:** To investigate whether nonlinear dimensionality reduction improves unsupervised classification of  $^1\text{H}$  MRS brain tumor data compared with a linear method.

**Methods:** In vivo single-voxel  $^1\text{H}$  magnetic resonance spectroscopy (55 patients) and  $^1\text{H}$  magnetic resonance spectroscopy imaging (MRSI) (29 patients) data were acquired from histopathologically diagnosed gliomas. Data reduction using Laplacian eigenmaps (LE) or independent component analysis (ICA) was followed by k-means clustering or agglomerative hierarchical clustering (AHC) for unsupervised learning to assess tumor grade and for tissue type segmentation of MRSI data.

**Results:** An accuracy of 93% in classification of glioma grade II and grade IV, with 100% accuracy in distinguishing tumor and normal spectra, was obtained by LE with unsupervised clustering, but not with the combination of k-means and ICA. With  $^1\text{H}$  MRSI data, LE provided a more linear distribution of data for cluster analysis and better cluster stability than ICA. LE combined with k-means or AHC provided 91% accuracy for classifying tumor grade and 100% accuracy for identifying normal tissue voxels. Color-coded visualization of normal brain, tumor core, and infiltration regions was achieved with LE combined with AHC.

**Conclusion:** The LE method is promising for unsupervised clustering to separate brain and tumor tissue with automated color-coding for visualization of  $^1\text{H}$  MRSI data after cluster analysis. **Magn Reson Med 74:868–878, 2015.** © 2014 Wiley Periodicals, Inc.

**Key words:** pattern recognition; dimensionality reduction; Laplacian eigenmaps; magnetic resonance spectroscopy; magnetic resonance spectroscopic imaging

## INTRODUCTION

Gliomas are the most common type of primary brain tumor, and accurate diagnosis of tumor grade is necessary for appropriate treatment and prognosis. Histopathological characterization from a surgical biopsy carries risk (1,2) and can be problematic due to tumor heterogeneity (1,3,4). Conventional MRI provides limited accuracy in defining tumor heterogeneity and infiltration boundaries, and  $^1\text{H}$  magnetic

resonance spectroscopic imaging (MRSI) is being investigated for its clinical potential to aid noninvasive diagnosis (5). The manual interpretation and analysis of large multi-voxel  $^1\text{H}$  MRSI datasets is difficult and time-consuming, hence automated pattern recognition (PR) methods are being investigated for tumor classification (6–9). PR of MRSI data has shown promise in objectively delineating tumor boundaries and defining infiltrative growth patterns in gliomas (10,11) and nosologic images (3,12) used to summarize the presence of various tissue types and lesions in a single color-coded image overlay onto conventional MRI.

Prior to PR, dimensionality reduction (DR) is needed. DR provides a mathematical mapping of high dimensional data into a lower dimensional representation. In particular, lower dimensional representations ideally should be obtained without substantial loss in discriminative information, while maximally preserving overall data geometry. Consequently, points that are in close proximity in the original high-dimensional space are mapped to adjacent locations in the low-dimensional space (13). Principal component analysis (PCA) and independent component analysis (ICA) are well-known linear DR techniques that have been applied to  $^1\text{H}$  MRS data, but there are assumptions in their application. First, PCA will not extract the true variance from a non-Gaussian distribution of data, so is not ideal for super Gaussian or high-kurtosis sources. Second, ICA requires input data to be linear, independent, and non-Gaussian. ICA can outperform PCA, as the underlying probabilistic model is more powerful and is sensitive to higher-order statistics allowing superior identification of data concentrations in  $n$ -dimensional space (14). In contrast, nonlinear DR techniques (15–20) can unfold high-dimensional data that provide class separation where linear methods often fail.

In this study, we focused on the application of the nonlinear Laplacian eigenmaps (LE) method for DR of  $^1\text{H}$  MRS brain tumor data with the aim to aid diagnosis and determine regions of potential tumor infiltration. LE-DR was chosen due to the simplicity of its implementation and its robustness to outliers and noise (20). We used unsupervised, learning-based k-means and agglomerative hierarchical clustering (AHC) methods to form three clusters (nominally representing normal tissue, potential infiltration, and tumor core) determined from the eigenvalues of the DR output. Single-voxel MRS (SVS) and MRSI results obtained via LE-DR were compared with those obtained using PCA + ICA. We investigated the extent to which the nonlinear LE-DR method provides improved classification for generation of color-coded maps of tumor core, infiltration, and normal tissue compared with conventional linear DR.

Neurosciences Research Centre, Cardiovascular and Cell Sciences Institute, St. George's University of London, London, UK.

Grant sponsor: Cancer Research UK project; Grant number: C1459/A13303. Data were obtained during the EU FP7 eTUMOUR project.

\*Correspondence to: Guang Yang, Ph.D., Neurosciences Research Centre, Cardiovascular and Cell Sciences Institute, Room 31b, St George's, University of London, Cranmer Terrace, London, SW17 0RE. E-mail: gyang@sgul.ac.uk

Received 2 July 2014; revised 12 August 2014; accepted 18 August 2014

DOI 10.1002/mrm.25447

Published online 8 September 2014 in Wiley Online Library (wileyonlinelibrary.com).

© 2014 Wiley Periodicals, Inc.

868

Table 1

Number of Patients Studied and Number of Spectroscopic Voxels Analyzed for Each Tissue Class

	Tissue class				Total
	Grade II	Grade III	Grade IV	Normal	
No. of subjects studied					
Experiment 1: SV MRS	24	0	31	3	58
Experiment 2: MRSI	10	7	13	0	30
No. of MRS voxels analyzed					
Experiment 1: SV MRS	24	0	31	79	134
Experiment 2: MRSI	722	509	734	0	1965

For the SVS experiment, we applied our methods to 55 SV tumor spectra combined with 79 normal spectra derived from the MRSI data of three normal controls. For the MRSI experiment, we applied our method to 1965 2D chemical shift imaging spectra derived from grade II, grade III, and grade IV patients. No extra normal control data were added into the MRSI analysis, because the rectangular 2D chemical shift imaging grid included enough contralateral normal voxels from the tumor patients.

## METHODS

All MR data were acquired using a GE Signa Horizon 1.5T MR system (GE Healthcare, Milwaukee, Wisconsin, USA) equipped with 22 mT/m gradients and a quadrature head coil. Study participants gave written informed consent in accordance with local ethics procedures. Biopsy or resected tumor tissue samples were available to confirm histological tumor diagnosis providing a “ground truth” classification.

### SVS: Subjects and Data Acquisition

SVS data were acquired from adult brain tumor patients at St George’s, University of London, as part of the INTER-PRET and eTUMOUR EU projects (data are web-accessible by permission for download from <http://solaria.uab.es/eTumour/>). In total,  $N=55$  tumor MR spectra were obtained. This included 24 grade II tumors (2 oligodendrogliomas, 3 oligoastrocytomas, 3 fibrillary astrocytomas, 4 gemistocytic astrocytomas, and 12 diffuse astrocytomas) and 31 grade IV tumors (31 glioblastomas). To create a dataset of normal brain single-voxel spectra, 79 spectra were extracted from MRSI data of three healthy volunteers, which had compatible repetition time (TR)/echo time (TE) parameters (full acquisition details as defined in the next section), and these data were interpolated to the same spectral resolution as the SVS tumor data. The final dataset comprised  $N=134$  individual spectra (Table 1).

All SVS tumor data were acquired at a short TE using the GE developed point-resolved spectroscopic sequence protocol (TR=2000 ms, TE=30 ms, 2048 data points with 2500 Hz bandwidth). Voxels for MRS were positioned according to the clinical MRI of each patient to predominantly include viable tumor tissue and avoid areas of pure necrosis. Each spectrum was referenced to both *N*-acetyl-aspartate (NAA) at 2 ppm (search region=2.20–1.80 ppm) and choline (Cho) at 3.21 ppm (search region=3.30–3.12 ppm) for chemical shift alignment. In addition, each spectrum was truncated to 4.0–0.2 ppm containing  $M=198$  data points representing the majority of metabolic information (Fig. 1a).

### MRSI Chemical Shift Imaging: Subjects and Data Acquisition

Our thirty  $^1\text{H}$  MRSI data were obtained from 29 patients with grade II (2 oligoastrocytomas, 2 gemistocytic astro-

cytomas, 6 diffuse astrocytomas), grade III (1 anaplastic oligoastrocytoma, 6 anaplastic astrocytomas), and grade IV (1 gliosarcoma, 12 glioblastomas) glial tumors. For one patient diagnosed with an anaplastic astrocytoma, postsurgical resection MRSI data were acquired 15 wk after the initial scan, and both pre- and postsurgery scans were included in the study.

MRSI data were acquired using the GE PROBE-SI protocol (TR=2000 ms, TE=30 ms, 512 data points, and 1000 Hz bandwidth) with outer volume suppression and a  $16 \times 16$  phase-encoded matrix. A 15-mm thick axial plane was selected through the center of the tumor mass with a selection volume for MRSI that included the tumor bulk and surrounding tissue while avoiding the skull. MRSI data were preprocessed by zero-filling prior to two-dimensional (2D) Fourier transformation to produce a  $32 \times 32$  matrix of voxels with in-plane spatial resolution of 6.875 mm. In addition, zero-filling was applied to each free induction decay signal in the Fourier domain, interpolating the original 512 data points to 2048. This provided high-resolution spectra while preserving relative metabolite signal intensities.

A total of  $N=2097$  voxels were extracted from the MRSI data, but 132 voxels (6%) were excluded due to poor water suppression and misalignment (i.e., signals unable to be referenced as mentioned above), leaving  $N=1965$  voxels remaining (Table 1). Spectral data were limited (4.0–0.2 ppm), and the phased real part was used for further analysis. Each MRSI spectrum consisted of  $M=498$  data points (Fig. 1h).

### Pattern Recognition

#### Dimension Reduction

An in-house MATLAB program (MATLAB 2013a; Mathworks, Natick, Massachusetts, USA) was developed for processing, analysis, and display for the MR spectra. All SVS or MRSI spectra were stored as a 2D matrix,  $S \in \mathbb{R}^{M \times N}$ , where  $S = (s_1, s_2, \dots, s_N)$  contains each spectrum as a column vector  $s_n \in \mathbb{R}^M$ . The column vectors were normalized using

$$s_n^* = \frac{s_n}{\sqrt{\sum_m s_{nm}^2}} \quad \forall n \in \{1, 2, \dots, N\} \quad [1]$$

to form the matrix  $S^* \in \mathbb{R}^{M \times N}$ , in which  $N$  is the number of the spectra and  $M$  is the number of the data points of each spectrum.

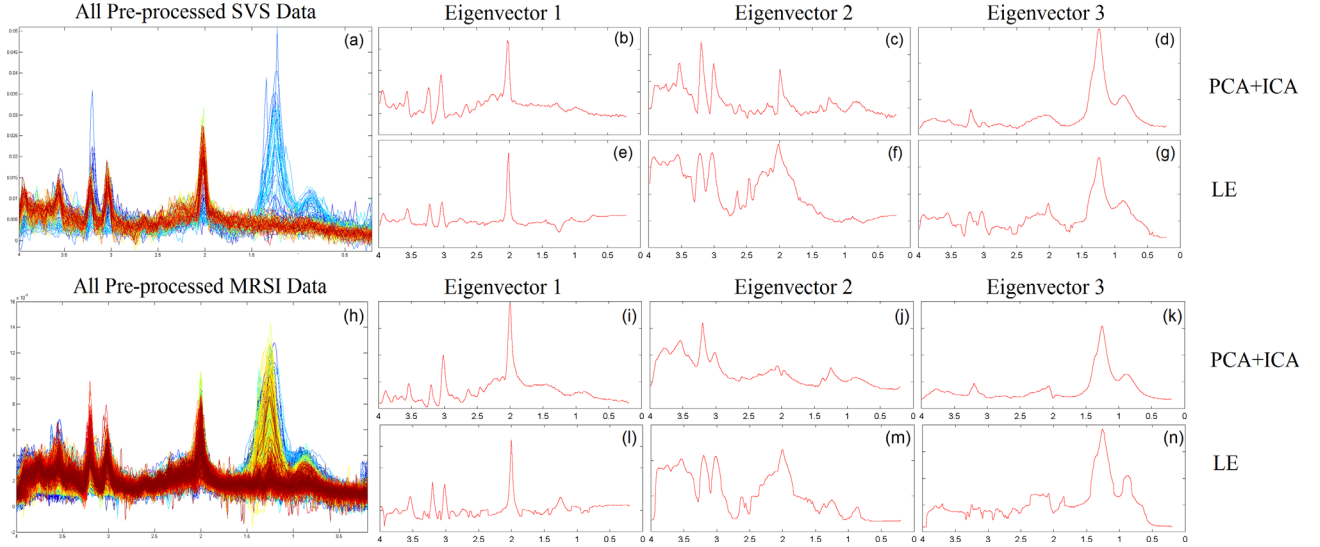


FIG. 1. Summary of preprocessed data and derived DR eigenvectors for SVS (a–g) and MRSI (h–n) data. All preprocessed SVS and MRSI spectra are shown overlain in panels a and h, respectively. For the SVS data, panels b–d show the three eigenvector components obtained after application of PCA + ICA and panels e–g show the three eigenvector components associated with the LE solution. For MRSI data analysis, the three independent components obtained after application of PCA + ICA are illustrated (i–k) with the three eigenvector components associated with the LE solution (l–n). The eigenvectors for each analysis are displayed in order for the tissue class they appear to represent: Eigenvector 1 = normal brain; Eigenvector 2 = grade II or infiltration; Eigenvector 3 = grade IV or necrotic tissue. All spectra are displayed with a 0–4 ppm x-axis and the spectra truncated to 0.2–4 ppm as used in the analysis.

We implemented the LE method (20), which assumes that data points lie on a smooth manifold that is a hyper-surface in high-dimensional space. In particular, LE computes a low-dimensional representation of the data that preserves local neighborhood information and reflects the geometric structure of the manifold. Subsequently, a weighted adjacency graph  $G$  with  $N$  nodes was constructed, in which each node represents a single spectrum in the dataset. To achieve this, the  $k$ -nearest neighbors method ( $k$ -NN) was applied to determine connectivity between the nodes according to the Euclidean distance in  $\mathbb{R}^N$ . Weights of connected edges was defined using a heat kernel:

$$W_{ij} = \begin{cases} \exp\left(-\frac{\|s_i^* - s_j^*\|}{\sigma^2}\right) & \text{if } s_i^* \text{ and } s_j^* \text{ are connected} \\ 0 & \text{otherwise} \end{cases} \quad [2]$$

The Laplacian matrix,  $L = D - W$ , was constructed in which  $W$  is the adjacency matrix defined in Equation [2] with the corresponding degree matrix,  $D_{ii} = \sum_j W_{ij}$ . Based on standard spectral graph theory, the matrix transformation,  $Y \in \mathbb{R}^{M \times N}$ , where  $Y = (y_1, y_2, \dots, y_n)$ , maps the weighted adjacency graph  $G$  to a low-dimensional space where connected nodes remain close together. This map is given by

$$\arg \min_y \sum_{ij} \|y_i - y_j\|^2 W_{ij}, \quad [3]$$

and provides heavy  $W_{ij}$  penalties if neighboring nodes  $s_i^*$  and  $s_j^*$  are mapped to be far apart. Minimization of Equation [3] attempts to ensure that if  $s_i^*$  and  $s_j^*$  are close, and

then the mappings  $y_i$  and  $y_j$  are similar. Furthermore, as  $D_{ii} = \sum_j W_{ij}$ ,  $W_{ij}$  is symmetric and  $L = D - W$ , we can derive the following:

$$\begin{aligned} & \arg \min_y \sum_{ij} \|y_i - y_j\|^2 W_{ij} \\ &= \arg \min_y \sum_{ij} (y_i^2 + y_j^2 - 2y_i y_j) W_{ij} \\ &= \arg \min_y \left( \sum_i y_i^2 D_{ii} + \sum_j y_j^2 D_{jj} - 2 \sum_{ij} y_i y_j W_{ij} \right) \\ &= \arg \min_y (2y^T L y) \equiv \arg \min_y \text{Tr}(Y^T L Y); \end{aligned} \quad [4]$$

therefore, the minimization problem may be simplified to

$$\arg \min_y \text{Tr}(Y^T L Y) \text{ subject to } Y^T D Y = I, \quad [5]$$

where  $L$  is positive semidefinite, thus the vector  $y$  that minimizes the objective function is given by the minimum eigenvalue solution to the generalized eigenvalue problem (with respect to eigenvalues,  $\lambda$ ) as follows:

$$L y = \lambda D y. \quad [6]$$

The constraint  $Y^T D Y = I$  prevents collapse onto a subspace of dimension less than  $N - 1$  with the solution provided by the eigenvectors with the smallest non-zero eigenvalues (20).

For our LE-DR with further unsupervised clustering framework, we have no separate training dataset to optimize the two parameters ( $k$  in the  $k$ -NN algorithm and  $\sigma$  in the heat kernel function) in LE-DR. Recent studies have shown that  $k \approx \frac{1}{10}N$  is suitable for various applications (21,22) and that  $\sigma$  can be set according to the mean

distance between graph neighbors that is widely used in various nonlinear DR methods (23–25). Therefore, we set  $k=12$  and  $\sigma=0.45$  for  $N=134$  SVS, and  $k=200$  and  $\sigma=0.52$  for  $N=1965$  MRSI.

Our comparison for the LE-DR method is ICA, a linear blind source separation technique used to identify individual signals from mixtures (26), which in our study may resemble spectral patterns of the tissue subtypes in each MRS voxel (11). We employed the fastICA package (<http://research.ics.aalto.fi/ica/fastica>), which implements a fast fixed-point algorithm in MATLAB (27). Spectra were first normalized and mean-centered, and then PCA was applied prior to ICA to limit the number of independent components generated and to provide “whitening” of the data. Preprocessing the data using PCA enhances ICA performance by discarding small trailing eigenvalues and reduces computational complexity for the fastICA iterative algorithm by minimizing pairwise dependencies (28). In addition, PCA also de-correlates the input mixing data, and the remaining higher-order dependencies can be separated by ICA. Whitening ensures that all dimensions are treated equally a priori before the application of ICA. Three principal components were then derived, as this is the expected number of stable components in the glioma MRS dataset (11).

#### Unsupervised Learning Based Clustering

k-means is one of the most popular iterative-descent clustering methods (29). In our implementation, the sum of absolute differences was used as the dissimilarity measurement, with each centroid representing the component-wise mean of the points in that cluster. The cluster number was set to  $k=3$  under the assumption of the existence of three tissue classes representing normal brain, infiltrative tumor (grade II for the SVS analysis), and high-grade/necrotic tissue (grade IV for the SVS analysis).

For AHC, the Euclidean distance was used as a pairwise dissimilarity measure. A bottom-up paradigm was used to recursively merge pairs of clusters into a single cluster at each level (30). Pairs were merged based on the smallest inter-group dissimilarity.

#### Data Analysis

##### SVS Data Analysis

PCA + ICA and LE were applied to the SVS dataset and each spectrum was assigned a spectral classification label according to their ranked eigenvalues. Mean eigenvector spectra and variance were then calculated for identification of the tissue types represented by each spectral class.

k-means and AHC methods were used to segment the 3D eigenspace for each DR method. Quantitative validation was provided by mean silhouette values (31). For each k-means or hierarchical cluster, the cluster label was defined according to the metabolic characteristics of the mean cluster spectrum. Clustering performance was evaluated by accuracy, sensitivity, specificity and balanced error rate (BER) (32) computed with respect to “ground truth” histopathological diagnosis for each patient.

##### MRSI Data Analysis

The above analysis was also applied to the MRSI data. Results were visualized using color overlays (green = normal, blue = infiltrative, red = high-grade/necrotic) on conventional MRI to allow assessment of classification results in the absence of histopathological ground truth for all voxels in the MRSI dataset.

Because we have a small number of MRSI datasets for each tumor grade, and the components derived by data reduction will depend on the input dataset, we propose a take-one-out method for the MRSI analysis as an added estimate of the stability of the overall process of tissue segmentation by data reduction and clustering. This is unlike the standard leave-one-out process, and assesses the consistency of data clustering (in the absence of definitive tissue classification for every MRSI voxel) rather than the accuracy of classification. Cluster stability (CS) was defined as the percentage difference between classification labels of all MRSI voxels before and after one patient dataset was removed prior to the DR and clustering procedure. CS was computed separately for each tissue segment  $q \in \{1, 2, 3\}$  such that

$$CS_q = \sum_{\hat{p}} \frac{c(\hat{p}, q)}{\hat{n}} \times 100$$

$$\text{where } c(\hat{p}, q) = \begin{cases} 0 & \text{if } c(p) = q = c(\hat{p}) \\ 1 & \text{if } c(p) = q \neq c(\hat{p}) \end{cases}, \quad [7]$$

where  $c(p)$  is the voxel classification that is computed from the entire MRSI dataset and  $c(\hat{p})$  is the voxel classification computed over the set of MRSI voxels  $\hat{p} \in \{1, 2, \dots, \hat{n}\}$  after removal of one patient. Clustering performance was evaluated by CS and BER, which was computed by comparing color overlays with histopathological diagnosis for each patient.

## RESULTS

### Dimensionality Reduction

Figure 1 shows eigenvector results represented as spectra for DR by PCA + ICA (Fig. 1b–d) and LE (Fig. 1e–g) for SVS data and for MRSI data (Fig. 1i–n). Common spectral features were observed for the eigen-decomposed spectra derived by both DR techniques for both datasets. Eigenvector 1 (Fig. 1b,e,i,l) showed characteristic NAA, total creatine, total choline (tCho), and mI peaks in proportions typical of normal brain tissue. Eigenvector 3 (Figure 1d,g,k,n) showed the absence of NAA and includes large lipid/macromolecules signals at 1.3 and 0.9 ppm, which are characteristic of tumor core with necrotic regions in high-grade tumors. Eigenvector 2 showed elevated mI and reduced NAA for all DR results (Fig. 1c,f,j,m) and is likely associated with the presence of glial cells and neuronal cell loss found in infiltrative tumor regions. For the PCA + ICA analysis there were also elevated tCho (Figure 1c,j). Eigenvector 2 showed less consistency across all analyses but had characteristics that can be associated with grade II gliomas and regions of tumor infiltration. Overall, there appeared to be more consistency between



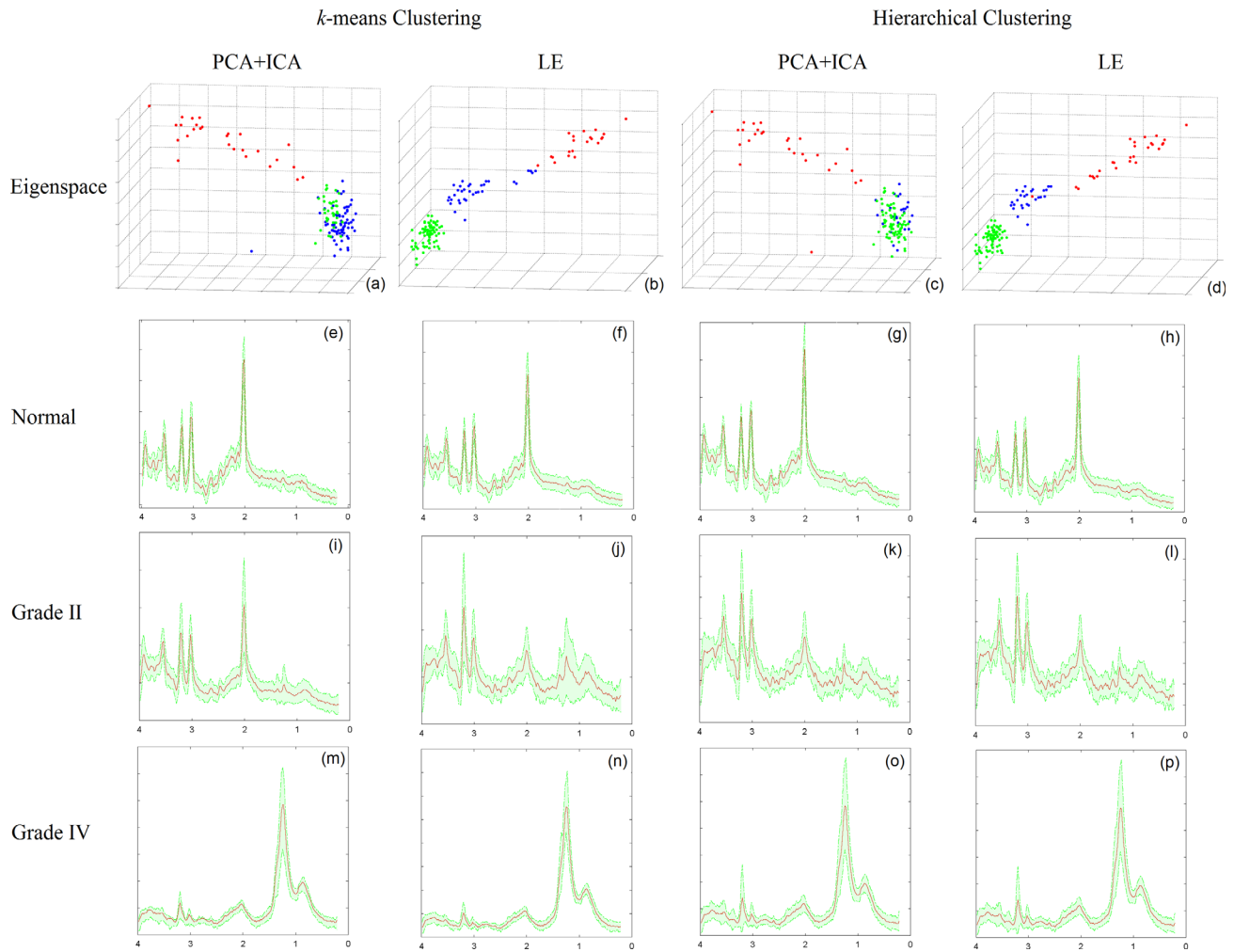


FIG. 2. SVS data clustering results (a–d) and mean spectra for the various clusters (e–p). Scatter plots show the results of k-means (a and b) and agglomerative hierarchical clustering (c and d) when applied to PCA + ICA (a and c) and LE-DR (b and d). Color-coding of the scatter plots is according to the tissue class most likely associated to the mean spectra of each cluster (e–p): green = normal brain tissue; blue = grade II; red = grade IV. Mean (solid red curve) and one standard deviation (dashed green curves) spectra are illustrated below each scatter plot. All spectra are displayed with a 0–4 ppm x-axis and the spectra are truncated to 0.2–4 ppm as used in the analysis.

the two spectroscopic datasets for the eigenvectors derived by LE-DR than by PCA + ICA.

#### SVS Data Cluster Analysis

Figure 2a–d shows eigenvalue scatter plots colored according to cluster group (green = normal brain tissue, blue = grade II, red = grade IV). Cluster group assignment was based on the similarity of their mean metabolite spectra (Fig. 2e–p) to the known spectra of normal brain and the mean spectra of gliomas of different grades as found in other brain tumor studies (33,34) and is shown for the current single voxel data in Figure 3a–c. For the purpose of labeling, Figure 2i was also assigned as grade II, and although it closely resembled normal brain spectra, there were slightly elevated tCho and the presence of a small lactate doublet, both of which are grade II characteristics. The scatter plots show that LE-DR increased the separation between tissue classes by unfolding the data into a more linear distribution compared with

PCA + ICA. This particularly affects the combination of PCA + ICA with k-means, which does not make such a clear separation of the metabolic characteristics of normal tissue and low-grade tumors as shown by the mean and standard deviation spectra (Fig. 2e,i).

Both clustering methods have significantly lower mean silhouette widths after PCA + ICA than LE-DR (Wilcoxon signed-rank test,  $P < 0.001$ ) (Table 2) indicating the presence of data outliers. Better clustering after LE-DR is potentially attributable to unfolding of the original high-dimensional data into a more linear low-dimensional data structure.

Smaller classification errors were obtained for k-means clustering by LE than by PCA + ICA, whereas low classification errors were found for AHC after both DR techniques (Table 2). Normal spectra were only misclassified by the combination of k-means clustering and PCA + ICA. The improved classification by k-means after LE-DR was indicated by higher sensitivity and specificity for classification of normal and grade II tumors (Table 3).

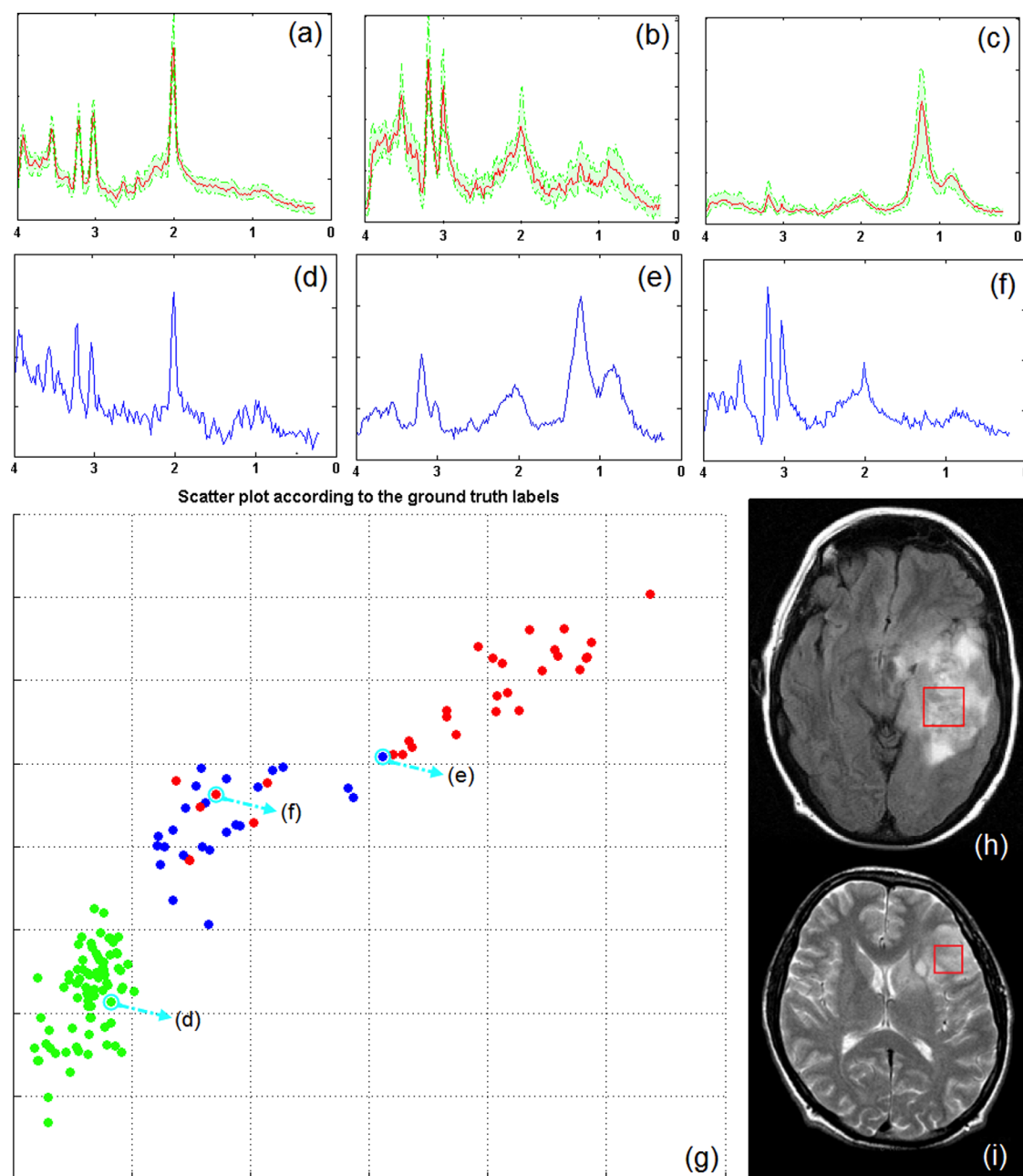


FIG. 3. Assessment of the LE-DR clustering of the SVS experiment with respect to the clinical- and histological-based “ground truth.” **a–c:** The mean (solid red curves) and standard deviation (dashed green curves) spectra are shown for 79 normal (a), 24 grade II (b), and 31 grade IV (c) classes. **d–f:** Nontypical cases of a normal spectrum with a grade II feature of elevated Cho to Cr ratio due to baseline distortion (d), a grade II tumor spectrum with prominent grade IV features (e), and a grade IV tumor spectrum with no lipid signals and therefore grade II characteristics (f). **g:** These atypical spectra are indicated within the LE-DR scatter plot, which is color-coded according to “ground truth” labels: green = normal brain tissue, blue = grade II; red = grade IV. **h:** FLAIR image of the grade II case depicted in panel e. **i:** T<sub>2</sub>-weighted image of the grade IV case depicted in panel f. The planned SVS location is indicated by a red box in both cases. All spectra are displayed with a 0–4 ppm x-axis and the spectra are truncated to 0.2–4 ppm as used in the analysis.

The mean and standard deviation spectra for the tissue classes according to histopathologically classification of a biopsy are shown in Figure 3a–c and were similar to the spectra derived from all the DR and cluster analyses except for that derived by PCA + ICA with k-means (Fig. 2i). Examples of outlying spectra were identified for normal tissue (Fig. 3d), grade II gemistocytic astrocytoma (Fig. 3e), and grade IV glioblastoma (Fig. 3f). The normal

spectra were generally well clustered in the LE-DR eigen-space (Fig. 3g), even for a normal spectrum with low-grade characteristics of elevated choline to creatine due to the rising baseline from poor water suppression (Fig. 3d). Inconsistency between diagnosis and classification was found in the grade II and grade IV cases. Here, the outlying grade II spectrum (Fig. 3e,h) had high-lipid components and was misclassified as grade IV. The

Table 2  
Evaluation of All Methods for SVS Data

Test	k-Means clustering		AHC	
	PCA + ICA	LE	PCA + ICA	LE
Silhouette analysis (SVS)	0.4 ± 0.3	<b>0.6 ± 0.2</b>	0.5 ± 0.2	<b>0.6 ± 0.2</b>
Tumor versus normal classification (SVS), %	67	<b>100</b>	<b>100</b>	<b>100</b>
Classification accuracy/BER (SVS), %	60/30	<b>93/11</b>	<b>93/11</b>	<b>93/11</b>

A total of 55 patients with 55 tumor spectra plus 79 spectra extracted from three healthy controls using MRSI were evaluated. Bold values indicate the best performer or best performers if all equal.

grade IV glioblastoma spectrum (Fig. 3f,i) had no lipid component and was misclassified as grade II.

#### MRSI Data Cluster Analysis

Eigenvalue scatter plots in Figure 4a–d show the LE method to provide a more linear distribution of eigenvalues than the PCA + ICA method in accordance with the SVS data (Fig. 2a–d). For each DR technique, both k-means and AHC methods showed similar clustering characteristics (as seen by comparing Fig. 4a and 4c or Fig. 4b and 4d). Mean spectra of the clusters for all four methods show similarities for normal tissue characteristics (Fig. 4e–h) and high-grade necrotic core (Fig. 4m–p) as found using SVS data (Fig. 2e–h and Fig. 2m–p). Differences in mean spectra were found in the cluster and are potentially attributable to low-grade tumor characteristics (PCA + ICA, Fig. 4i,k; LE-DR, Fig. 4j,l). Here, the PCA + ICA mean spectra had a slight reduction in NAA and elevation in tCho that were more likely associated with grade II tumor infiltrative regions. The LE-DR mean spectra had a greater elevation in tCho, greater reduction in NAA, and presence of lipid and macromolecules peaks (1.3 and 0.9 ppm) and so would be associated with infiltration that also includes some high-grade tumor regions. For the purposes of labeling, we refer to this as the tumor infiltration cluster.

Visualization of AHC results overlain on conventional MRI allowed the anatomical locations of segmented tissue types to be assessed visually. Six exemplary cases are illustrated in Figure 5 showing two grade II tumors (n = 1 diffuse astrocytoma [Fig. 5a,g]; n = 1 gemistocytic astrocytoma [Fig. 5b,h]), two grade III tumors (n = 2 anaplastic astrocytomas), and two grade IV tumors (n = 2 glioblastomas). For seven of the 30 MRSI data sets, PCA + ICA misclassified normal tissue voxels that were distant from or contralateral to the main lesion as tumor (Table 4) for k-means (data not shown) and for AHC (Fig. 5).

To provide an assessment of the accuracy of AHC techniques for correctly identifying patients with low-grade (grade II) or high-grade (grade III and IV) tumors, each patient MRSI color map was considered to represent a high-grade tumor if any voxel was colored red (i.e., high-grade/necrotic core) and low-grade if only colored blue or green (i.e., the infiltration cluster). Good accuracy and low BER (better than for the SVS data) was achieved for all analysis combinations for grade II versus grade IV classification (Table 4). However, the inclusion of grade III in the high-grade group reduced classification performance (Table 4). Cystic regions in grade II and grade III cases were graded as high-grade by PCA + ICA (Fig. 5a,d) due to the presence of lactate, which was effectively misinterpreted as a lipid component in the data reduction. This is in contrast to LE-DR, where all cystic

Table 3  
Quantitative Validation of Clustering Techniques on DR Results of SVS Experiment with Respect to Histopathological “Ground Truth”

	Predicted Group Membership				Sensitivity, %	Specificity, %
	Normal	Grade II	Grade IV	Total		
k-Means clustering						
PCA + ICA						
Normal	35	44	0	79	44	100
Grade II	0	21	3	24	88	54
Grade IV	0	7	24	31	77	97
LE-DR						
Normal	79	0	0	79	100	100
Grade II	0	24	0	24	100	91
Grade IV	0	10	21	31	68	100
Hierarchical clustering						
PCA + ICA						
Normal	79	0	0	79	100	100
Grade II	0	21	3	24	88	95
Grade IV	0	6	25	31	81	97
LE-DR						
Normal	79	0	0	79	100	100
Grade II	0	21	3	24	88	95
Grade IV	0	6	25	31	81	97

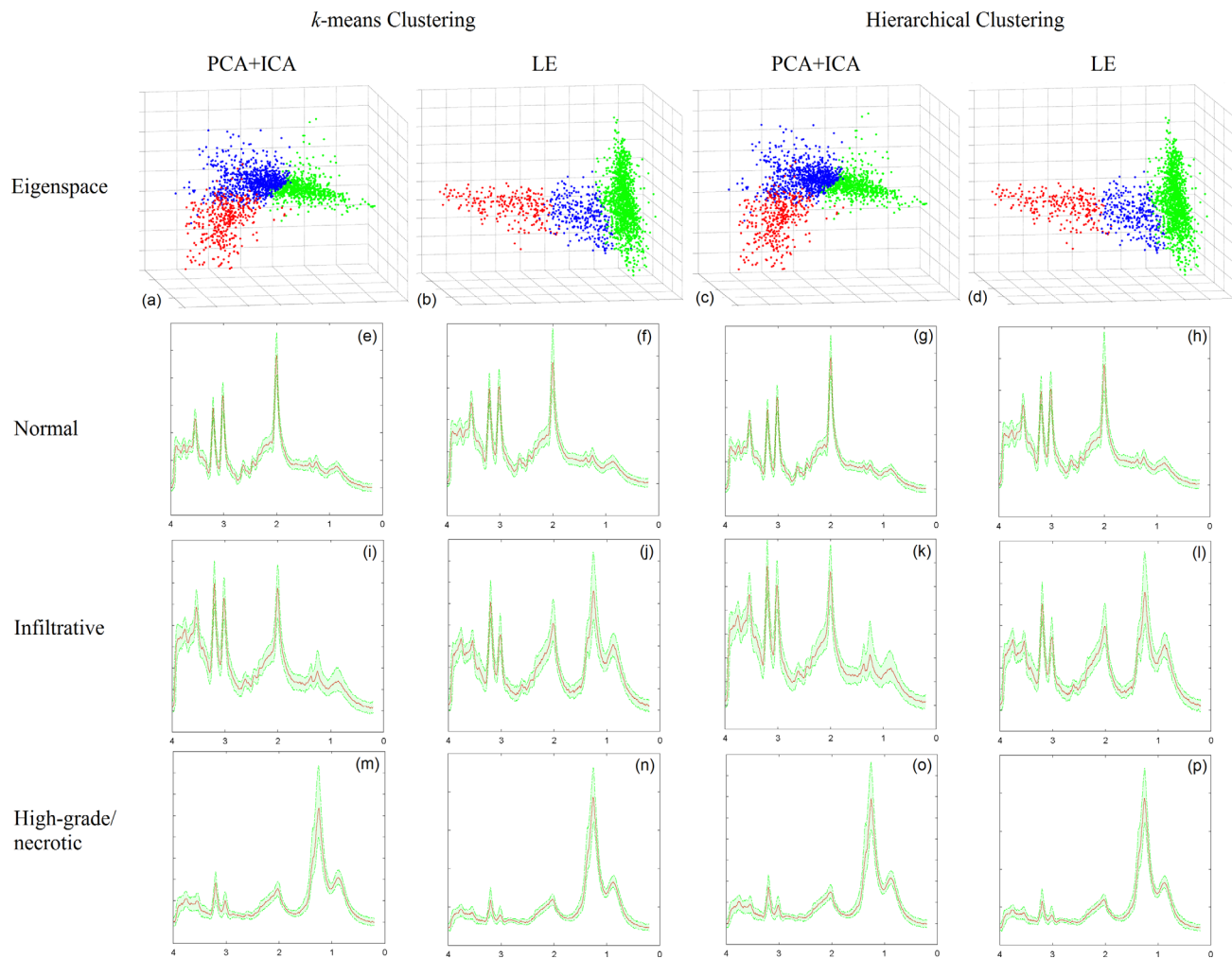


FIG. 4. MRSI data clustering results (a–d) and mean spectra for the various clusters (e–p). Scatter plots show the results of k-means (a and b) and agglomerative hierarchical clustering (c and d) when applied to PCA + ICA (a and c) and LE-DR (b and d). Color-coding of the scatter plots is according to the tissue class most likely associated to the mean spectra of each cluster (e–p): green = normal brain tissue, blue = infiltrative tumor, red = high grade tumor/necrotic core. Mean (solid red curve) and one standard deviation (dashed green curves) spectra are illustrated for the clusters underneath each scatter plot. All spectra are displayed with a 0–4 ppm x-axis and the spectra are truncated to 0.2–4 ppm as used in the analysis.

regions were clustered and classified as infiltration regions. Hence, there was a higher BER for grade II versus grade IV classification with PCA + ICA than for LE-DR (Table 4). Conversely, the grading of cystic regions in some grade III tumors as high-grade by PCA + ICA (Fig. 5d) provided slightly higher classification accuracy compared with LE-DR for grade II tumors versus grade III and grade IV tumors (Table 4).

The best performance across all measures (Table 2 and Table 4) was achieved by LE-DR with AHC. In general, this provided anatomically reasonable classification of low-grade regions within (Fig. 5h) or up to the edge of the  $T_2$ -weighted MRI abnormality (Fig. 5g). For high-grade tumors, there is generally a core region (red) surrounded by an infiltrative (blue) margin that extends beyond the post-gadolinium  $T_1$ -weighted margin (Fig. 5k) or lies within the  $T_2$ -weighted hyperintense region (Fig. 5l). Grade III tumors were mixed in terms of these characteristics (Fig. 5i,j).

## DISCUSSION

In this study, we developed a new metric to qualitatively and quantitatively characterize brain tissue into normal, tumor infiltration, and tumor core segmentations using a nonlinear one-step DR by LE on  $^1\text{H}$  MRS data. Overall, our results suggest that an LE-DR + AHC framework provides improved tissue classification compared with conventional linear PCA + ICA with k-means methods. The classification results of the SVS analysis also suggest the visual segmentations provided by MRSI color overlays for necrotic tumor core and infiltration have validity (Fig. 5g–l).

A limitation of the current MRSI study is that in vivo multiple-voxel data have no histopathological validation available on a voxel-by-voxel basis. The gold standard of brain tumor diagnosis is histopathological analysis of a biopsy, with the highest grade tumor cells determining the clinical grade and subsequent patient treatment.



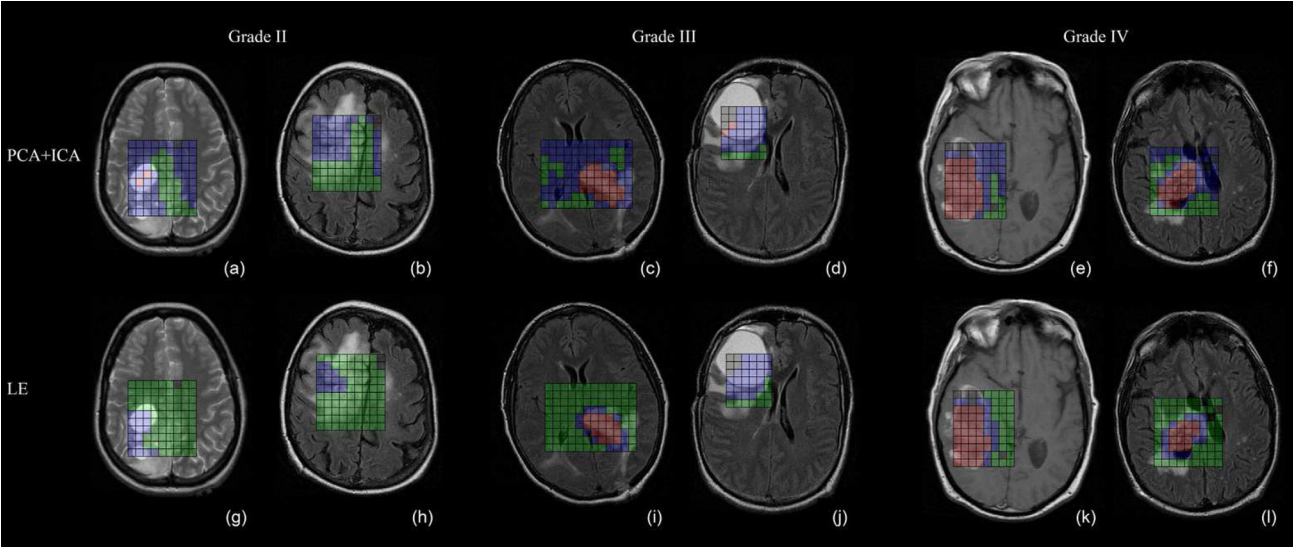


FIG. 5. RGB overlays on conventional images showing the tissue group assigned to the spectrum in each MRSI voxel after agglomerative hierarchical clustering of the complete MRSI dataset. The top row illustrates results using PCA + ICA and the bottom row shows results using LE-DR data. Two grade II cases (left two columns), two grade III cases (middle two columns), and two grade IV cases (right two columns) are shown. Green = normal brain, blue = infiltrative tumor, red = high-grade/necrotic tumor. Noncolored voxels within the MRSI grid were removed by our quality control criteria.

However, this may not fully represent the average tumor characteristic over large MRS voxels. Consequently, errors in “ground truth” may affect classifier derivation and accuracy evaluation (35). With our unsupervised classification, we have found that for both SVS and MRSI data, LE-DR provides a natural clustering of spectra that agrees well with the clinical and histopathological diagnosis of grade II and grade IV gliomas and to the anatomical extent of these tumors by MRI (Fig. 5). The apparent grade II regions surrounding a grade IV core (Fig. 5k,l) have been observed in other MRSI studies (3,11). Partial volume of high-grade tumor core with surrounding infiltrative tumor will lead to a continuum of spectral characteristics; hence with unsupervised clustering of the MRSI data there is some mixing of the grade II and high-grade necrotic spectra (Fig. 4j,l) with LE-DR. However, this appears less of a problem in terms of classification and characterization (Table 4) than the effects of partial volume mixing of grade II and normal tissue when using PCA + ICA data reduction (Fig. 4i,k).

Classification of grade III tumors remains a challenge due to heterogeneous tumor characteristics. In this study, we assumed the existence of three distinct tissue components. In a preliminary study (data not shown), four LE components were tested but provided no added benefit

in tumor tissue classification, with the additional subclass representing partial volume of gray and white matter regions.

Although we may expect a linear signal path from tissue metabolite concentration to MRS signal intensity and that spectra from mixed tissue types will add in linear proportion, our results suggest benefits for application of nonlinear data analysis techniques. In the presence of large heterogeneity found in tumors and adjacent brain tissue, there is no reason to suppose simple linear functions will provide the best relationship between MR spectrum (visual data) and tissue class (world state) (36). The LE method provides very narrow eigenvector spectral peaks for normal brain components (Fig. 1e) and broader peaks for tumor (Fig. 1f,g) in contrast to PCA + ICA (Fig. 1b–d). This suggests that LE-DR is potentially detecting factors associated with nonlinear effects in metabolite line shape in tumor tissue. Nonlinear effects also occur due to distortions in relative metabolite peak heights for peripheral MRSI voxels due to chemical shift artifacts; however, in the current study, these were reduced by excluding outer edge voxels of the MRSI volume. Variations in metabolite line width and nonlinear variations in peak height may be caused by heterogeneity of tumor tissue. Necrosis, fibrosis, edema, and hemorrhage may all

Table 4  
Evaluation of All Methods for MRSI Data

Test	k-means Clustering		AHC	
	PCA + ICA	LE-DR	PCA + ICA	LE-DR
Cluster stability (MRSI), %	10 ± 19	2 ± 1	5 ± 2	<b>1 ± 1</b>
Normal tissue misclassified as grade II (MRSI)	Yes (7/30)	<b>No</b>	Yes (7/30)	<b>No</b>
Grade II versus grade IV accuracy/BER (MRSI), %	<b>91/9</b>	<b>91/8</b>	<b>91/9</b>	<b>91/8</b>
Grade II versus grade III + grade IV accuracy/BER (MRSI), %	<b>77/20</b>	<b>73/20</b>	<b>77/20</b>	<b>73/20</b>

Data are presented for 30 patients with 1965 voxels. Bold values indicate the best performer or best performers if all equal.

contribute to microscopic magnetic field inhomogeneities at the cellular level and cause larger scale heterogeneity across the MRSI volume and spectrum distortions.

The LE-DR method appears to unfold the MRS data to a more linear data structure than PCA + ICA. A consequence of this is a more linear geometry for data clustering that leads to better cluster stability following LE-DR than PCA + ICA. It is apparent that LE-DR unfolds the MRS data into a structure of spectral characteristics from normal brain to high-grade tumor characteristics that provides improved classification accuracies and lower error rates.

Our classification accuracies of 93% with SVS and 91% with MRSI for distinguishing grade II from grade IV tumors compares well with other PR analyses. Classification accuracy of 93% has been obtained by combining long-echo and short-echo spectra (37); however, this would be difficult to routinely achieve due to time constraints. A more recent approach used nonnegative matrix factorization to accomplish the DR task for SV tumor spectra (38); however, nonnegative matrix factorization methods converge to local minima, and various initializations provide different DR, thus requiring an elaborate initialization scheme (38). Ortega-Martorell et al. reached 22% BER with long-echo SVS and 7% BER with short-echo SVS for supervised classification of grade II, grade IV, and normal spectra (38). In contrast, our unsupervised learning framework, which requires minimum parameter manipulation and no additional supervised training procedure, obtained the best classification accuracy for LE-DR + AHC with an 11% BER for SVS and an 8% BER for MRSI data. Further work with a more supervised approach to defining the clusters from LE-DR should achieve improved classification, but needs validation, such as with appropriately localised biopsy classification (39) or from longitudinal studies to confirm the presence of tumor infiltration and grade from tumor growth characteristics and patient outcome (40).

## CONCLUSION

This work presents a threefold contribution to automated analysis of brain tumor  $^1\text{H}$  MRS data. First, to the best of our knowledge, this is the first time a nonlinear DR method has been applied to MRSI data. Second, we have demonstrated a one-step DR using nonlinear LE in comparison to ICA (which relies on data preprocessing using PCA). LE-DR reduces the risk of loss of relevant data features and leads to better classification accuracy and clustering stability measures. Third, promising brain tissue segmentations have been achieved using LE-DR with unsupervised clustering of the data. Clustering using k-means or hierarchical algorithms and color visualization techniques indicate the possible benefits for the nonlinear LE-DR method in determining different MRS characteristics for low- and high-grade gliomas and for identifying infiltration into normal brain tissue. With further validation, these techniques could aid targeted biopsies and improve surgical and radiotherapy planning.

## REFERENCES

- Hall WA. The safety and efficacy of stereotactic biopsy for intracranial lesions. *Cancer* 1998;82:1749–1755.
- Favre J, Taha JM, Burchiel KJ. An analysis of the respective risks of hematoma formation in 361 consecutive morphological and functional stereotactic procedures. *Neurosurgery* 2002;50:48–56.
- De Edelenyi FS, Rubin C, Estève F, et al. A new approach for analyzing proton magnetic resonance spectroscopic images of brain tumors: nosologic images. *Nat Med* 2000;6:1287–1289.
- Jackson RJ, Fuller GN, Abi-Said D, Lang FF, Gokaslan ZL, Shi WM, Wildrick DM, Sawaya R. Limitations of stereotactic biopsy in the initial management of gliomas. *Neuro Oncol* 2001;3:193–200.
- Howe FA, Opstad KS.  $^1\text{H}$  MR spectroscopy of brain tumours and masses. *NMR Biomed* 2003;16:123–131.
- Tate AR, Majós C, Moreno A, Howe FA, Griffiths JR, Arús C. Automated classification of short echo time in vivo  $^1\text{H}$  brain tumor spectra: a multicenter study. *Magn Reson Med* 2003;49:29–36.
- Devos A, Lukas L, Suykens JAK, et al. Classification of brain tumours using short echo time  $^1\text{H}$  MR spectra. *J Magn Reson* 2004;170:164–175.
- Simonetti AW, Melssen WJ, De Edelenyi FS, van Asten JJ A, Heerschap A, Buydens LMC, De Edelenyi FS. Combination of feature-reduced MR spectroscopic and MR imaging data for improved brain tumor classification. *NMR Biomed* 2005;18:34–43.
- Georgiadis P, Kostopoulos S, Cavouras D, Glotsos D, Kalatzis I, Sifaki K, Malamas M, Solomou E, Nikiforidis G. Quantitative combination of volumetric MR imaging and MR spectroscopy data for the discrimination of meningiomas from metastatic brain tumors by means of pattern recognition. *Magn Reson Imaging* 2011;29:525–535.
- De Edelenyi FS, Simonetti FA, Postma WG, Huo R, Buydens LMC. Application of independent component analysis to  $^1\text{H}$  MR spectroscopic imaging exams of brain tumours. *Anal Chim Acta* 2005;544:36–46.
- Wright AJ, Fellows G, Byrnes TJ, Opstad KS, McIntyre DJO, Griffiths JR, Bell BA, Clark CA, Barrick TR, Howe FA. Pattern recognition of MRSI data shows regions of glioma growth that agree with DTI markers of brain tumor infiltration. *Magn Reson Med* 2009;62:1646–1651.
- Luts J, Laudadio T, Idema AJ, Simonetti AW, Heerschap A, Vandermeulen D, Suykens JAK, Van Huffel S. Nosologic imaging of the brain: segmentation and classification using MRI and MRSI. *NMR Biomed* 2009;22:374–390.
- Lee JM. Riemannian manifolds: an introduction to curvature. New York: Springer; 1997.
- Bartlett MS, Movellan JR, Sejnowski TJ. Face recognition by independent component analysis. *IEEE Trans Neural Netw* 2002;13:1450–1464.
- Schölkopf B, Smola A, Müller K-R. Nonlinear component analysis as a kernel eigenvalue problem. *Neural Comput* 1998;10:1299–1319.
- Tenenbaum JB, De Silva V, Langford JC. A global geometric framework for nonlinear dimensionality reduction. *Science* 2000;290:2319–2323.
- Law MHC, Jain AK. Incremental nonlinear dimensionality reduction by manifold learning. *IEEE Trans Pattern Anal Mach Intell* 2006;28:377–391.
- Roweis ST, Saul LK. Nonlinear dimensionality reduction by locally linear embedding. *Science* 2000;290:2323–2326.
- Saul LK, Roweis ST. Think globally, fit locally: unsupervised learning of low dimensional manifolds. *J Mach Learn Res* 2003;4:119–155.
- Belkin M, Niyogi P. Laplacian Eigenmaps for dimensionality reduction and data representation. *Neural Comput* 2003;15:1373–1396.
- Chen L, Tsang IW, Xu D. Laplacian embedded regression for scalable manifold regularization. *IEEE Trans Neural Netw Learn Syst* 2012;23:902–915.
- Wu R, Yu Y, Wang W. SCALE: Supervised and cascaded Laplacian eigenmaps for visual object recognition based on nearest neighbors. In: 26th IEEE Conference on Computer Vision and Pattern Recognition, Portland, OR, June 23–28, 2013. p. 867–874.
- De Silva V, Tenenbaum J. Global versus local methods in nonlinear dimensionality reduction. *Adv Neural Inf Process Syst* 2003;721–728.
- Charpiat G, Faugeras O, Keriven R, Maurel P. Distance-based shape statistics. *Acoust Speech Signal Process* 2006;5:925–928.
- Luxburg U. A tutorial on spectral clustering. *Stat Comput* 2007;17:395–416.
- Hyvärinen A, Karhunen J, Oja E. Independent component analysis. Hoboken, NJ: John Wiley & Sons; 2004.
- Hyvärinen A, Oja E. A fast fixed-point algorithm for independent component analysis. *Neural Comput* 1997;1492:1483–1492.

28. Draper BA, Baek K, Bartlett MS, Beveridge JR. Recognizing faces with PCA and ICA. *Comput Vis Image Underst* 2003;91:115–137.
29. MacKay D. An example inference task: clustering. In: *Information theory, inference and learning algorithms*. Cambridge, UK: Cambridge University Press; 2003. p. 284–292.
30. Press W, Teukolsky S, Vetterling W, Flannery B. Hierarchical clustering by phylogenetic trees. In: *Numerical recipes: the art of scientific computing*. New York: Cambridge University Press; 2007. p. 868–881.
31. Rousseeuw PJ. Silhouettes: a graphical aid to the interpretation and validation of cluster analysis. *J Comput Appl Math* 1987;20:53–65.
32. Chen Y, Lin C. Combining SVMs with various feature selection strategies. In: Guyon I, Nikravesh M, Gunn S, Zadeh LA, editors. *Feature extraction: foundations and applications*. Springer Berlin Heidelberg; 2006. p. 315–324.
33. Tate AR, Underwood J, Acosta DM, et al. Development of a decision support system for diagnosis and grading of brain tumours using in vivo magnetic resonance single voxel spectra. *NMR Biomed* 2006;19: 411–434.
34. Opstad KS, Ladrone C, Bell BA, Griffiths JR, Howe FA. Linear discriminant analysis of brain tumour 1H MR spectra: a comparison of classification using whole spectra versus metabolite quantification. *NMR Biomed* 2007;20:763–770.
35. Yang G, Raschke F, Barrick TR, Howe FA. Classification of brain tumour 1H MR spectra: extracting features by metabolite quantification or nonlinear manifold learning? In: *2014 IEEE 11th International Symposium on Biomedical Imaging (ISBI)*, Beijing, China, April 29 to May 2, 2014. p. 1039–1042.
36. Prince SJD. *Computer vision: models, learning and inference*, 1st edition. New York: Cambridge University Press; 2012.
37. García-Gómez J, Tortajada S, Vidal C. On the use of long TE and short TE SV MR spectroscopy to improve the automatic brain tumor diagnosis. Leuven, Belgium: Katholieke University Leuven; 2007.
38. Ortega-Martorell S, Lisboa PJG, Vellido A, Julià-Sapé M, Arús C. Non-negative matrix factorisation methods for the spectral decomposition of MRS data from human brain tumours. *BMC Bioinformatics* 2012;13:38.
39. McKnight TR, von dem Bussche MH, Vigneron DB, Lu Y, Berger MS, McDermott MW, Dillon WP, Graves EE, Pirzkall A, Nelson SJ. Histopathological validation of a three-dimensional magnetic resonance spectroscopy index as a predictor of tumor presence. *J Neurosurg* 2002;97:794–802.
40. Wald LL, Nelson SJ, Day MR, et al. Serial proton magnetic resonance spectroscopy imaging of glioblastoma multiforme after brachytherapy. *J Neurosurg* 1997;87:525–534.